



## Synthesis of magnetic Fe–carbon nanohybrid for adsorption and Fenton oxidation of tetracycline

Hassan Yadaei<sup>a,b</sup>, Mostafa Nowroozi<sup>a</sup>, Mostafa Hossein Beyki<sup>a</sup>, Farzaneh Shemirani<sup>a,\*</sup>, Siavash Nouroozi<sup>b</sup>

<sup>a</sup>School of Chemistry, University College of Science, University of Tehran, P.O. Box: 14155-6455, Tehran, Iran, emails: shemiran@khayam.ut.ac.ir (F. Shemirani), hassanyadaie@gmail.com (H. Yadaei), mostafa\_nowroozi@yahoo.com (M. Nowroozi), hosseinbakim@gmail.com (M.H. Beyki)

<sup>b</sup>Department of Chemistry, University of Zanjan, Zanjan 45195-313, Iran, email: s.nouroozi@znu.ac.ir

Received 24 November 2018; Accepted 26 July 2019

### ABSTRACT

This work focuses on developing an efficient water decontaminant system based on magnetic carbon nanohybrid. To achieve this goal,  $\text{MnFe}_2\text{O}_4$  nanoparticles were synthesized by simple coprecipitation method then nitrogen-doped polyphenol resin was prepared by cross-linking of phenylenediamine and resorcinol over  $\text{MnFe}_2\text{O}_4$  nanoparticles. The prepared magnetic composite was heat treated in an argon atmosphere at  $800^\circ\text{C}$  for 2 h. Characterization of the heat treated nanohybrid with XRD revealed that the iron oxide phase changed to zero-valent iron nanoparticles. Moreover, transmission electron microscopy image, and Brunauer, Emmett and Teller analysis confirmed that the nanohybrid possesses a mesoporous structure with the surface area of  $153.1\text{ m}^2/\text{g}$ . Prepared nanohybrid was employed for tetracycline removal from aqueous solution with adsorption and Fenton oxidation processes. Effective parameters on the adsorption process such as pH, time, adsorbent dosage, ionic strength and  $\text{H}_2\text{O}_2$  amount were optimized with response surface methodology. For the adsorption process, kinetic models were also studied within 7 min of equilibrium time. Results confirmed that tetracycline adsorption followed the pseudo-first-order kinetic model. Isotherm study showed that Freundlich model can better describe the adsorption process moreover Dubinin–Radushkevich model showed the adsorption is a physical process. The maximum adsorption capacity of  $103\text{ mg/g}$  was obtained. Fenton oxidation can effectively increase the removal percentage since at an initial concentration of  $100\text{ mg/L}$ , the removal efficiencies were 28.5% and 91.8% by the adsorption experiment and Fenton process, respectively.

*Keywords:* Tetracycline; Mesoporous carbon; Magnetic composite; Fenton oxidation; Response surface method

### 1. Introduction

Presence of pharmaceuticals in the water resources and wastewater is a growing concern in the recent decades since about 3,000 different types of pharmaceuticals such as antibiotics and painkiller compounds are used extensively worldwide in human therapy and the farming industry all over the world [1,2]. Among various types of care products

antibiotic compounds that are used extensively in human therapy, livestock husbandry, and aquaculture have been proved to be a class of potent pollutants. However, antibiotics such as tetracycline (TC) are cost-effective and have high quality as well as a desirable antimicrobial activity but they have a toxic nature towards aquatic organisms, which can affect the environmental sustainability [3–5]. TC in the water resources have the potential to foster the selection of resistant bacteria and resistance genes besides they metabolized

\* Corresponding author.

partially in the body of animals or people as a result thrown of the huge volume of them in water and effluents causes vast contamination of environmental matrixes [6]. Therefore, there is a great need to develop an effective treatment technique to eliminate TC before releasing them into the aquatic environment.

So far, various techniques have been developed for the removal of TC including coagulation–sedimentation, reverse osmosis, nanofiltration, ozonation, and biodegradation. In practice, the mentioned methods have a good performance in the removal of TC [7]; however they show some general drawbacks such as high cost and accumulation of concentrated sludge. Some of the mentioned methods such as biodegradation are only suitable for biodegradable tetracyclines or chemical oxidation has unsatisfactory removal efficiency in a low concentration of TC [8,9]. Among various available methods, adsorption is an effective technology for the treatment of low concentration of antibiotics [10]. The most widely reported adsorbents for antibiotic removal in the past decades include activated carbon, clay, resins, and biochar [11]. In recent decades, much attention has been devoted to the nano-structure materials as efficient adsorbents for pollutants removal owing to their unique stability, high capacity, and low cost [12,13].

Among different nanostructures, mesoporous carbons have attracted much attention as adsorbents for organic and inorganic pollutants because of their large specific surface area, chemical inertness, biocompatibility, and high thermal stability [14]. A large variety of synthesis strategies have been explored for the elaboration of porous carbon materials through either straightforward routes or more complex synthetic approaches. Among the various non-exhaustive synthesis routes, one may mention the template-directed synthesis or hard and soft templating routes [15]. This strategy uses soft-template from self-assembly of amphiphilic block copolymers and phenolic resins, the ionothermal carbonization with ionic liquids [16] and the synthesis of hierarchically porous carbons in deep eutectic solvents [17]. In fact, in the soft template method, synthetic polymers with tunable and predictable properties are used as carbon precursors which can better control the properties of the mesoporous carbon [18,19]. Moreover, this operation mode is a large-scale production mode of mesoporous carbons for adsorption of water pollutants. Most of the mesoporous carbons have some practical drawbacks in aqueous media which include a high hydrophobic characteristic of their surface and a limited number of specific active sites [20]. It was found that the incorporation of nitrogen and other heteroatoms into the carbon lattice can improve properties of the mesoporous materials. In fact, nitrogen doping enhances the surface polarity and electron-donor tendency of the mesoporous carbons, which enables their application in various fields [21]. In view of water treatment application, carbon powders in water cause secondary pollution. Hence after adsorption of the pollutant from the liquid sample, it is necessary to separate the adsorbent from the medium. This can be conventionally performed by filtration or centrifugation which is rather time-consuming and expensive [22]. To make this process feasible, magnetic adsorbents can be employed since can be attracted from aqueous media with a simple external magnetic field [23]. Among various magnetic

nanoparticles,  $\text{MnFe}_2\text{O}_4$  as a soft magnetic material has been investigated in recent years for their high magnetic permeability, chemical, and corrosive stability, low cost, and environmentally friendly characteristics [24]. The magnetic nanoparticles not only facilitate adsorbent collection from reaction vessel but also have the potential for the oxidation and sorption of tetracycline simultaneously [25,26]. In fact, the presence of octahedral sites containing  $\text{Fe}^{2+}$  ions in the ferrite structure enhances the production rate of hydroxyl radical through Fenton catalytic process [27].

Based on the aforementioned notes, this work exhibits an efficient removal system for tetracycline adsorption/oxidation based on magnetic mesoporous carbon. Magnetic  $\text{MnFe}_2\text{O}_4$  nanoparticles were used as core materials and covalently bonded polyphenol was employed as a precursor to prepare mesoporous material. Effective parameters on TC removal including pH, contact time, adsorbent dosage, and  $\text{H}_2\text{O}_2$  amount were optimized with response surface methodology (RSM) using Box–Behnken design. Isotherm and the kinetic study were also performed and discussed in detail.

## 2. Experimental

### 2.1. Materials and instruments

$\text{Fe}(\text{NO}_3)_3 \cdot 9\text{H}_2\text{O}$ ,  $\text{Mn}(\text{NO}_3)_2 \cdot 4\text{H}_2\text{O}$ , and NaOH were used to prepare  $\text{MnFe}_2\text{O}_4$  nanoparticles. Aminopropyltriethoxysilane (APTES), resorcinol, 1,4-phenylenediamine, p-formaldehyde (FA) and ethanol (Merck, Darmstadt, Germany) were applied for nanocomposite preparation. TC was supplied from Iranian quality control laboratory (Tehran, Iran).  $\text{H}_2\text{O}_2$  (35%) was used for the oxidation process.

Structure characterization of the materials was performed by powder X-ray diffraction analysis (XRD), field emission scanning electron microscopy (FESEM) and transmission electron microscopy (TEM), Fourier transforms infrared spectra (FTIR) and vibrating sample magnetometry (VSM). XRD was recorded with Phillips (Eindhoven, Netherlands) powder diffractometer, X' Pert MPD, using Cu-K $\alpha$  radiation at  $\lambda = 1.540589 \text{ \AA}$  (step size of 0.026, 40 kV and 40 mA). FESEM (kV = 25) and elemental mapping carried out using SIGMA VP ZEISS. The TEM analysis was performed with JEM-2010, Japan (80 kV). To prepare the sample for TEM analysis, it was ultrasonically (Misonix-S3000) dispersed in water and the resulting suspension dropped on a carbon-coated copper Mesh 300. FTIR was measured with Equinox 55 Bruker (Karlsruhe, Germany) at the wave-number of 400–4,000  $\text{cm}^{-1}$ . VSM was recorded with MDKFD instrument, Kashan, Iran, in the magnetic field of  $\pm 10 \text{ kOe}$  at 25°C. A digital pH meter (model 692, Metrohm, Herisau, Switzerland) was used for the pH adjustment. Brunauer, Emmett and Teller  $\text{N}_2$  adsorption–desorption isotherms (BET), and Barrett, Joyner and Halenda (BJH) pore size distribution were recorded on a Nova Station A system (outgas temperature: 150°C, sample weight: 0.28 g, analysis gas: nitrogen, outgas time: 6.0 h, bath temperature: 77.3 K, press. tolerance: 0.100/0.100 (ads/des), equal time: 60/60 s (ads/des)).

### 2.2. Synthesis of nanoparticles, polymer, and nanocomposite

To prepare magnetic  $\text{MnFe}_2\text{O}_4$  nanoparticles about 1.0 g of  $\text{Mn}(\text{NO}_3)_2 \cdot 4\text{H}_2\text{O}$  and 2.3 g of  $\text{FeCl}_3 \cdot 6\text{H}_2\text{O}$  were dissolved

in 200 mL distilled water. Then, 2.0 g of NaOH in 50 mL distilled water was dropped in the mixture and stirred for 5 min (final pH = 11). The mixture was sonicated at 80°C for 30 min then collected with external magnetic field, washed with distilled water and dried at 80°C for 12 h. To synthesize magnetic polymer, 0.5 g of  $\text{MnFe}_2\text{O}_4$  was added to 100 mL ethanol containing 1.0 g of phenylenediamine and 1.0 g of resorcinol along with stirring. After 30 min, 0.5 mL of APTES and 0.3 g of FA was added to the mixture. The mixture was refluxed for 24 h at 80°C along with magnetic stirring. At the end of the reaction, the product was separated by an external magnetic field and washed with ethanol and distilled water and dried at 80°C for 6 h. The prepared raw magnetic polyphenolic material was heated at 800°C in a furnace for 2 h under argon atmosphere.

### 2.3. TC adsorption/oxidation process

The prepared nanocomposite was employed for adsorption as well as oxidation of TC antibiotic. Effective parameters of the adsorption process were including pH (A), contact time (B) and adsorbent dosage (C). Effective parameters on the oxidation process were catalyst dosage (A), contact time (B) and  $\text{H}_2\text{O}_2$  amount (C) which were optimized with RSM. Experimental range levels and independent variables are presented in Table 1. Experiments were performed by 17 designed runs at one block using BBD (Design-Expert software version, 7.0.0). Based on RSM, a polynomial equation was used for the prediction of response as a function of significant variables and their interactions (Eq. (1)). The equations were validated by the analysis of variance (ANOVA) as well as 3D response surface plots drawn from the experimental data to overview the variables effects and optimum level of parameters.

$$Y = \beta_0 + \sum_{i=1}^k \beta_i X_i + \sum_{i=1}^k \beta_{ii} X_i^2 + \sum_{i=1}^{k-1} \sum_{j=2}^k \beta_{ij} X_i X_j + \sum_{i=1}^{k-1} \sum_{j=2}^k \beta_{ij} X_i^2 X_j \quad (1)$$

where  $Y$  is the predicted response;  $X_i$  and  $X_j$  represent the coded values of independent variables, and  $\beta$  is the regression coefficient constant of the developed model. TC sample volumes were 20 mL and its concentration was 10 and 100  $\text{mg L}^{-1}$  for adsorption and oxidation, respectively. Isotherm and kinetic studies were performed at optimum conditions for different concentrations of TC. In a typical run, the pH of the solutions was adjusted at optimum value then the optimum amount of the sorbent/catalyst (mg) was added to each flask. After shaking for an appropriate time (min), the solid mass was separated and the concentration of TC in the supernatant was determined by UV–Vis spectrophotometer. Removal percentage (%R) and adsorption capacity ( $Q \text{ mg g}^{-1}$ ) were calculated as follows:

$$\%R = \frac{(C_0 - C_e) \times 100}{C_0} \quad (2)$$

$$Q = \frac{(C_0 - C_e) \times V}{M} \quad (3)$$

Table 1

Experimental range levels and independent variables for TC removal by the adsorbent

	Variable	–1 level	+1 level
Adsorption	pH	2	9
	Time	1	15
	Dosage	5	15
	Ionic strength	1	5
	Time	1	10
Oxidation	Dosage	0	10
	$\text{H}_2\text{O}_2$	0	0.5

In these equations  $C_0$  and  $C_e$  ( $\text{mg L}^{-1}$ ) represent initial and remaining TC in the solution after equilibrium, respectively.  $V$  is sample volume (mL) and  $M$  is adsorbent/catalyst dosage (mg).

## 3. Results and discussions

### 3.1. Characterization

The crystalline structure of the synthesized  $\text{MnFe}_2\text{O}_4$  polymer nanocomposite and the magnetic carbon composite was studied with XRD analysis (Fig. 1). The XRD pattern of  $\text{MnFe}_2\text{O}_4$  shows typical peaks of a spinel structure at  $2\theta = 29.6^\circ, 35.1^\circ, 42.5^\circ, 52.7^\circ, 56.2^\circ,$  and  $61.7^\circ$  which can be assigned to (220), (311), (400), (422), (511), and (440) planes of ferrite nanoparticles (JCPDS no. 01-074-2403). The magnetic polymer nanocomposite exhibited two main

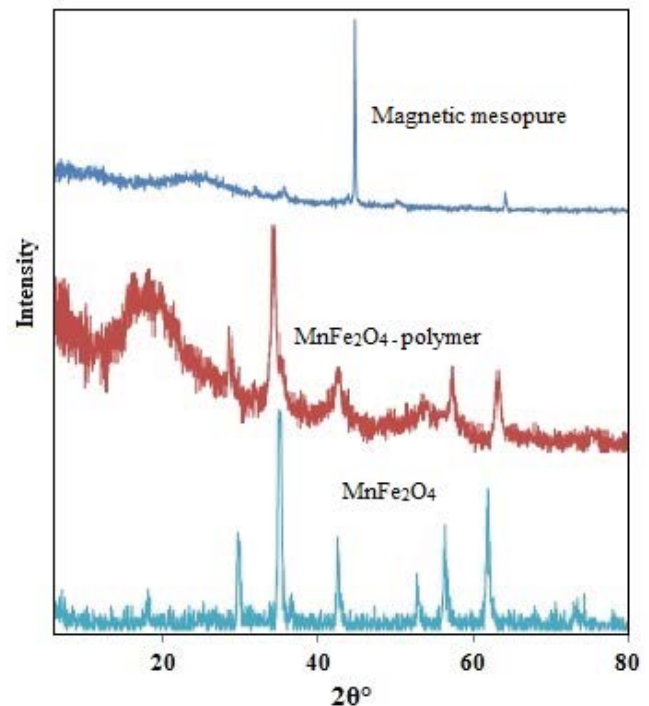


Fig. 1. XRD pattern of magnetic  $\text{MnFe}_2\text{O}_4$  precursor, and nanocomposite.

peaks at  $2\theta$  equal to  $10^\circ$  and  $22^\circ$  corresponding to the (001) and (110) pseudo-orthorhombic reflections of the aromatic backbone of polymer ascribed to periodicity parallel to the polymer chain [28]. The characteristic peaks of the ferrite nanoparticles are still observable in the XRD spectrum of magnetic nanocomposite with good intensity and confirmed that the crystalline behavior of the ferrites is not hampered by the deposited polymer on the surface of the nanoparticles.

After heat treatment of the magnetic nanocomposite, a main change in the XRD pattern is observed with appearing of a new sharp peak at  $2\theta$  equal to  $45^\circ$ . This is owing to the phase change of the magnetic oxide to zero-valent metal nanoparticles corresponding to 110 planes of the metallic Fe (JCPDS card no. 06-0696). In this work, ferrite oxide nanoparticles covered with silica and polymer then was used as the precursor to prepare magnetic carbon composite. Metal oxides and silica can act as acid catalysts to promote the thermal cracking process of carbon source materials. At this process, asymmetric breakage of carbon-hydrogen bonds yields hydride anions that are highly unstable and undergo processes of chain rearrangement and intra- and intermolecular hydrogen transfer. In other words, hydrogen ( $H_2$ ) is one of the main residuals of the cracking process which induces iron reduction from  $Fe^{3+}$  in the oxide structure to zero-valent iron nanoparticles [29].

Scherrer equation was employed to determine the average crystallite size of magnetic nanoparticles.

$$D = \frac{(0.9\lambda)}{(\beta \cos\theta)} \quad (4)$$

In this equation,  $D$  is the average crystal size,  $\lambda$  (0.1540589 nm) is the X-ray wavelength used,  $\beta$  (0.0011) is the angular line width of half maximum intensity in radians, and  $\theta$  ( $22.35^\circ$ ) is Bragg's angle expressed in degree. According to this equation, the average size of 138 nm was obtained for the nanoparticles.

The magnetic hysteresis loops for the precursor and prepared magnetic carbon composite are presented in Fig. 2a. The magnetic parameters include saturation magnetization ( $M_s$ ) and remnant magnetization ( $M_r$ ). The values of  $M_s$  for  $MnFe_2O_4$ -polymer was 10.15  $emu\ g^{-1}$  which increased to 27.06  $emu\ g^{-1}$ . This result can be assigned to phase change of the magnetic ferrite nanoparticles which is along with the reduction of iron oxide and generation of metallic Fe nanoparticles. It can be seen that the  $M_s$  value for the magnetic carbon composite is smaller than the  $M_s$  value of pure zero-valent iron (170–220  $emu\ g^{-1}$ ) [30]. The decrease in  $M_s$  value is dependent on the volume fraction of the magnetic nanoparticles, and on the contribution of the coating layer to the total magnetization. Additionally, it is observed that the  $M_r$  of the precursor is changed from 0.19 to 0.62  $emu\ g^{-1}$ , after heat treatment which indicates that the particles likely possess superparamagnetic or paramagnetic properties, because the remanence of the particles is near to zero in the absence of an external magnetic field [31]. However, the  $M_r/M_s$  ratio lies in the range of paramagnetic behavior ( $0 \leq M_r/M_s \leq 1$ ) [32].

The IR spectrum of magnetic polymer (Fig. 2b) shows several peaks at 890; 1,112; 1,441; 1,618; 2,951; 3,367; and 3,600  $cm^{-1}$ . The peak at 890 and 2,951  $cm^{-1}$  can be assigned to =C-H out-of-plane bending deformation in benzenoid aromatic ring and CH stretching [33]. The peak corresponding to the C=C group of aromatic backbone appeared at 1,441  $cm^{-1}$ . Moreover, OH and NH stretching are observed at 3,300–3,600  $cm^{-1}$  [34]. The peak at 1,112  $cm^{-1}$  corresponds to Si-O vibration. Relative to the spectrum of magnetic polymer, the FTIR spectra of the mesoporous compound show some changes. The peaks intensity are decreased after heat treatment and show two main peaks at 1,020 and 1,587  $cm^{-1}$  corresponding to Si-O, and C=C stretching vibration [35].

Fig. 3 shows the FESEM image of  $MnFe_2O_4$  magnetic polymer and mesoporous compound. It can be seen at Fig. 3a that manganese ferrite composed of nano-scale clusters which are an agglomeration of very fine nanoparticles with

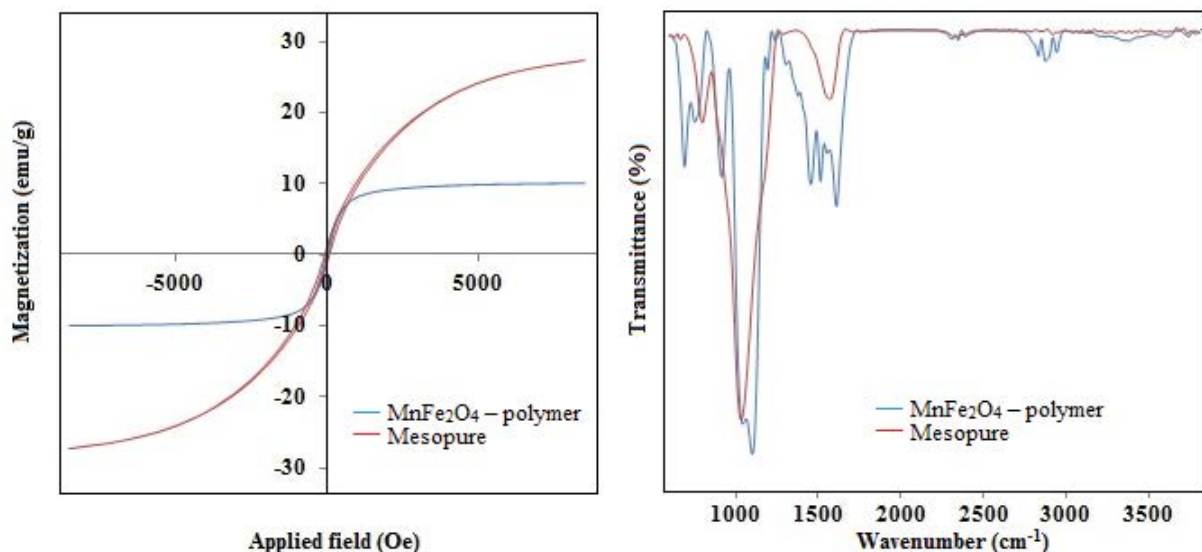


Fig. 2. VSM (a) and FTIR (b) analysis of precursor and nanocomposite.

a diameter of 20–30 nm. Cluster formation is owing to the intramolecular hydrogen bonding as the basis of cohesion between the nanoparticles. Figs. 3b and c show the FESEM image of the as-prepared magnetic polymer and mesoporous product. It indicated that the nanocomposite exhibited hyper-crosslinked structure with an aggregated fine sphere like nanoparticles. Formation of this type of structure is owing to the extended intra- and an intermolecular network of hydrogen bonds as a result of NH and OH groups as well as Van der Waals interaction between hydrophobic chains. The TEM images of the final product in Figs. 4a–c show porous structure after heat treatment as the pores are in nanoscale.

The  $N_2$  adsorption–desorption isotherm for the precursor and final composite is shown in Figs. 5a and b. As can be seen, the curve show type  $H_3$  isotherm with a minor hysteresis loop as a result of filling and emptying of the mesopores by capillary condensation [36]. As can be seen,

the lower limit of the desorption branch is normally located at the cavitation-induced  $p/p_0$ . Loops of this type represent non-rigid aggregates of plate-like particles as well as the pore network consists of macropores which are not completely filled with pore condensate [37]. The BET surface area of the magnetic polymer and mesoporous compound is 5.71 and 153.10  $m^2/g$ , respectively. Moreover, the pore means the diameter of the material is 13.80 and 7.64 nm. According to the pore size distribution, the materials are classified as mesoporous compounds [38]. Moreover, it was found that the total pore volume of the magnetic polymer is 0.019  $cm^3/g$  which increased to 0.292  $cm^3/g$  after heat treatment.

### 3.2. Fitting of the adsorption process models

The regression coefficients for the developed model was calculated with the BBD model and the empirical relationship

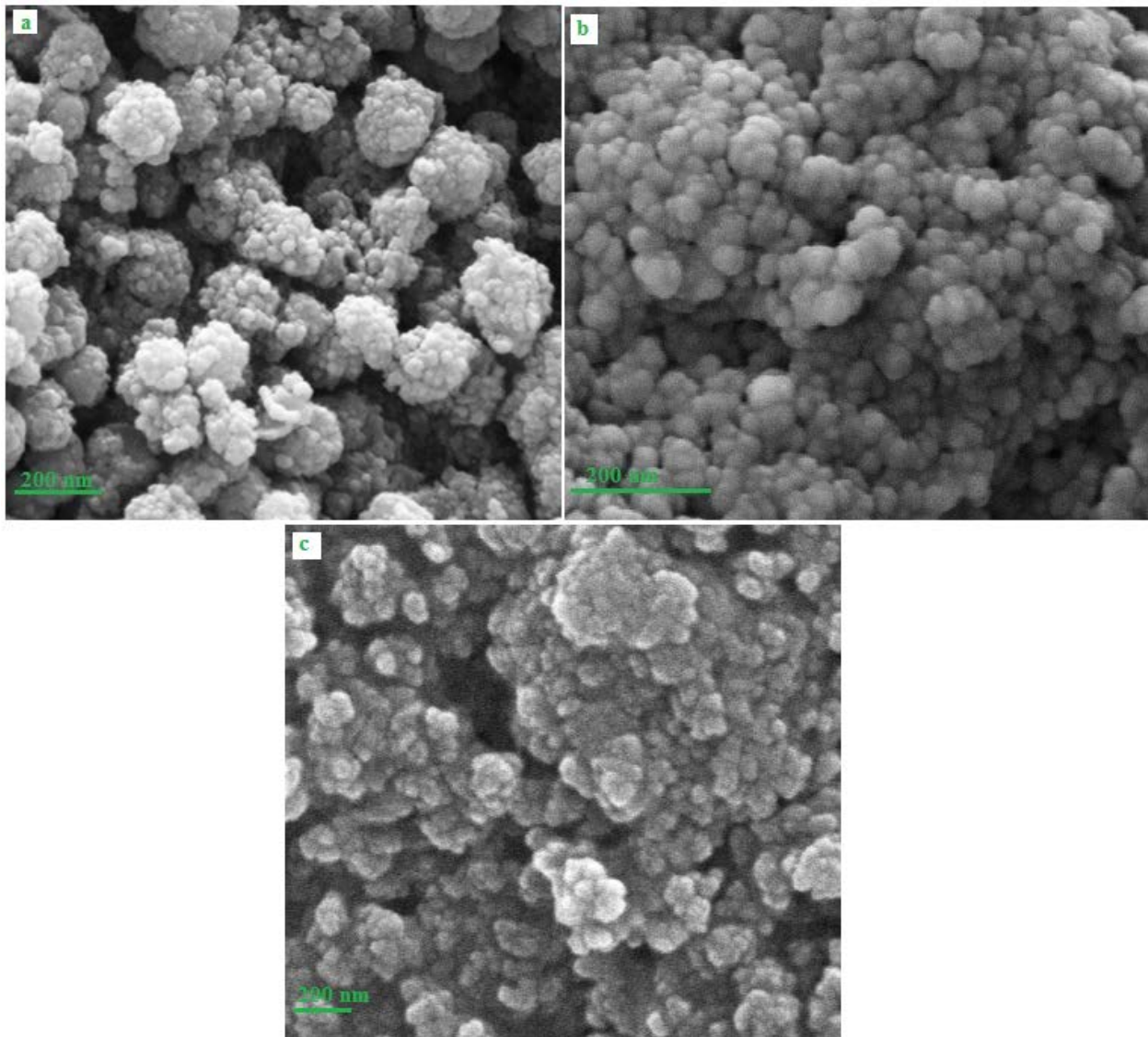


Fig. 3. FESEM image of  $MnFe_2O_4$  (a), precursor (b), and nanocomposite (c).

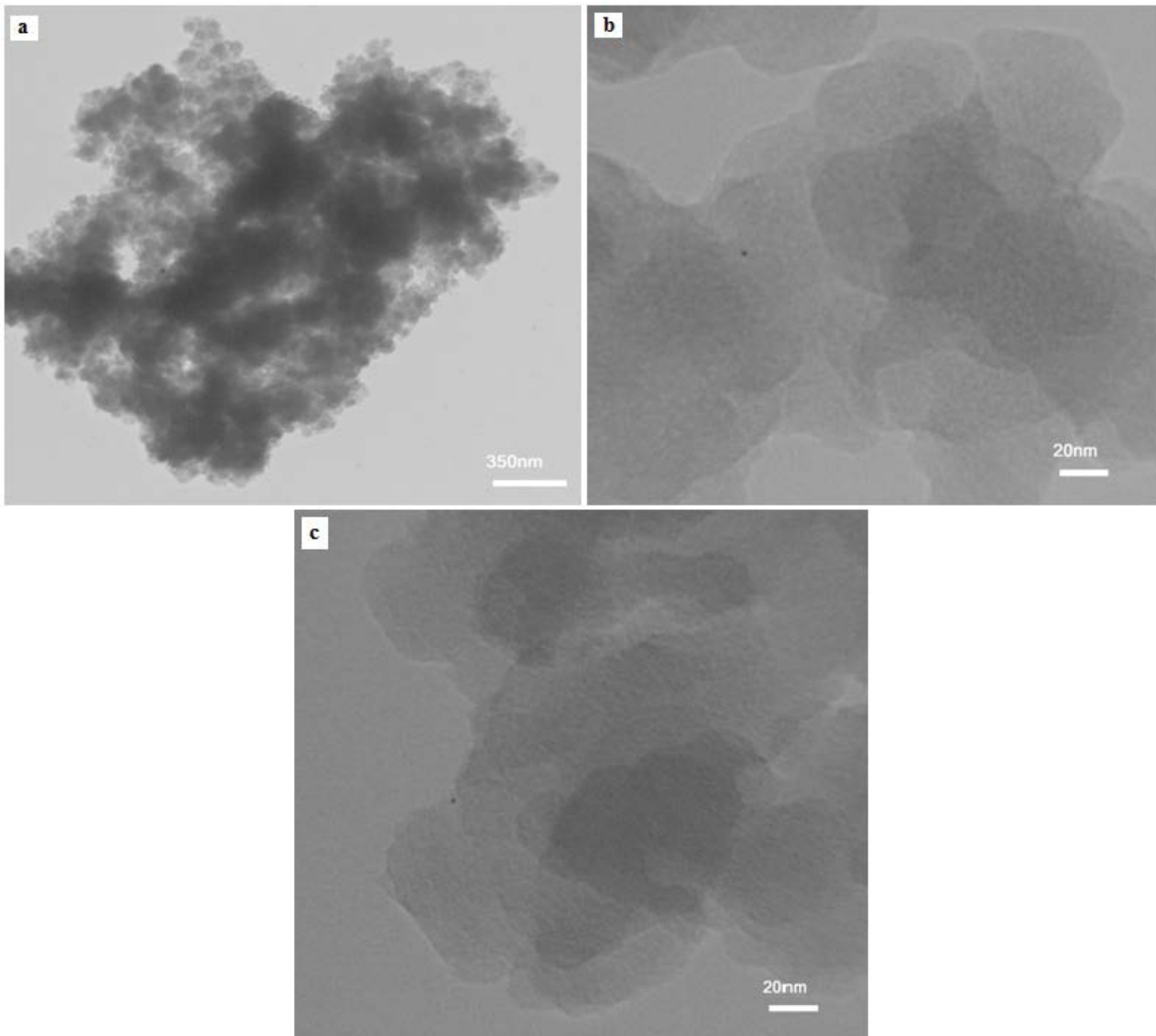


Fig. 4. TEM image of the nanocomposite.

between removal percentage ( $R\%$ ) and the variables were decoded. The equation is shown below:

$$\begin{aligned}
 R\% = & 85.89 - 3.46A + 2.5B + 6.33C - 1.82D + 1.13AB + 1.55AC \\
 & + 1.8AD - 1.81BC - 1.57BD + 4.22CD - 15.38A^2 - 2.57B^2 \\
 & + .65C^2 + 2.06D^2 + 4.47A^2B + 7.45A^2C - 1.59A^2D + 1.92AB^2 \\
 & - 0.85AC^2 - 3.5B^2C + 0.62B^2D - 0.69BC^2 \quad (5)
 \end{aligned}$$

In this equation,  $R\%$  is the response (removal percentage);  $A$ ,  $B$ ,  $C$ , and  $D$  are pH, contact time, sorbent dose, and ionic strength as independent variables. The ANOVA calculations were used to determine the significance of the coefficients (Table 2). It is noted that for any parameter to be a significant model component its  $F$  value should be higher and  $p$ -value (probability value) should be less than 0.05 [39,40]. The regressions for the adsorption of TC were statistically significant which is evident from the  $F$  values (53.86) with a low probability value ( $p < 0.0001$ ). Based on  $p$ -values of

each model term, the independent variables ( $A$ ,  $B$  and  $C$ ), interactive coefficients ( $CD$ ) and quadratic terms ( $A^2$ ,  $B^2$ ,  $D^2$ ,  $A^2B$ ,  $A^2C$ , and  $B^2C$ ) significantly affected the TC removal. The value of  $R^2$  (0.99) was in good agreement with adjusted  $R^2$  (0.97) and indicated a high dependence and correlation between the observed and the predicted values of the response. The adequate precision, signal to noise ratio, is 30.99 and demonstrated the significance of the adsorption model.

The validity of ANOVA was checked with a normal distribution of residuals from the normal probability plot (NPP) [41]. The NPP at Fig. 6a represents a straight line with low violation of the assumptions confirms the normality of the data. At perturbation plot (Fig. 6b) which shows the comparative effects of all media components on the response, steep curvature in pH ( $A$ ), time ( $B$ ), and dosage ( $C$ ) curve confirmed that TC adsorption process is very sensitive to these factors. From the relatively flat line

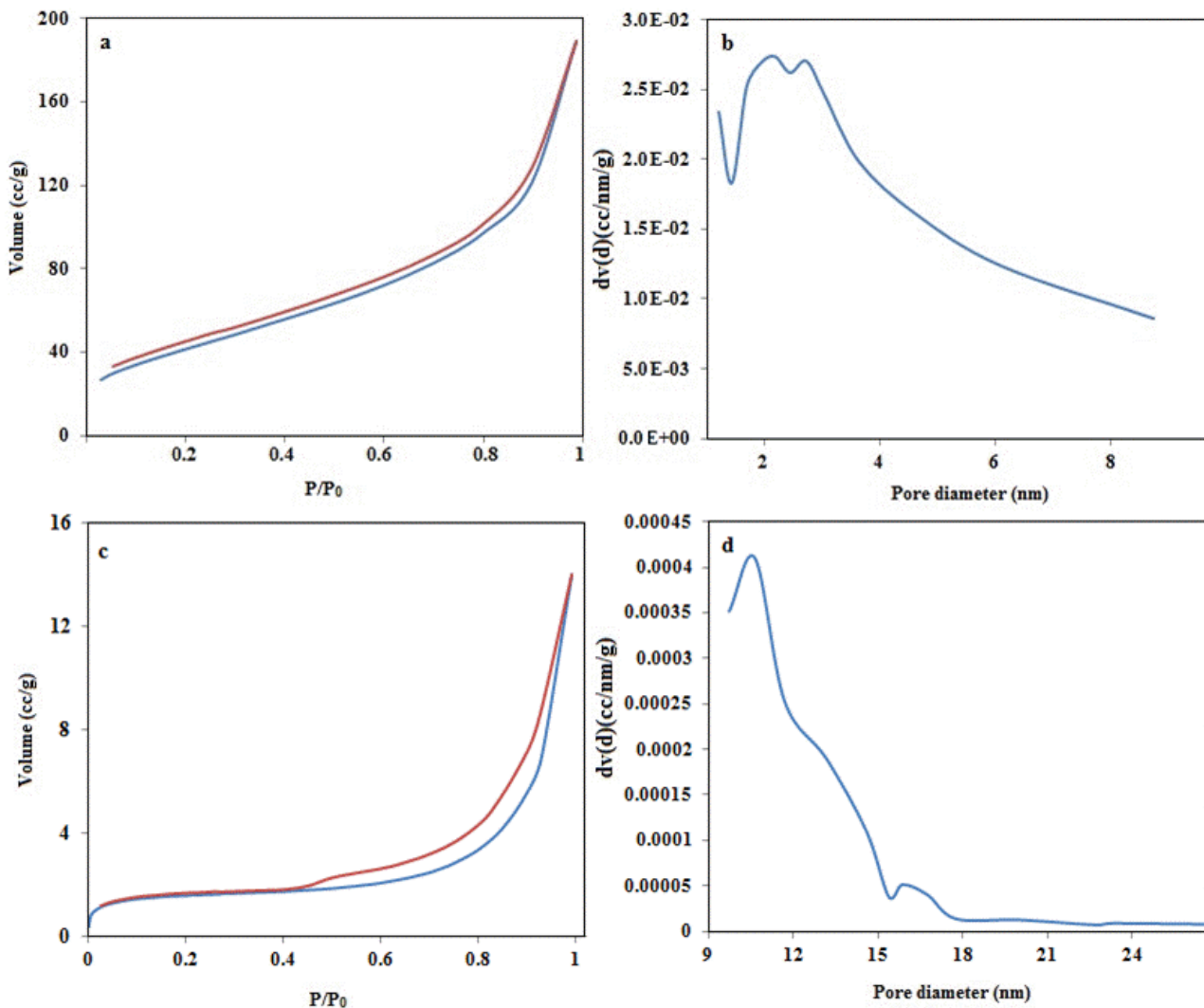


Fig. 5.  $N_2$  adsorption-desorption of precursor (a) and nanocomposite (c). BJH pore size distribution curves of precursor (b) and nanocomposite (d).

of the ionic strength ( $D$ ) can be concluded that the response is less sensitive to this variable. The relationship between the predicted value of the response (% $R$ ) with observed  $R$ % in Fig. 6c shows that most of the response points are located in a narrow range.

By taking removal percentage as the response, the three-dimensional response surfaces (Figs. 7 and 8) indicate the effects of selected parameters on the removal of TC. According to the results from the 3D plots, it can be seen that the removal percentage is very sensitive to pH since in the pH range from 2 to 5, mean removal efficiency was increased from about 50% to 95% then decreased with a further increase of pH up to 9. Contact time was designed in the range of 1–15 min. From the results, it can be seen that with increasing shaking time removal percentage was increased from 80% up to 95%. Time of 7 min was selected as the optimum level. This fast equilibrium time can be attributed to the availability and ease accessibility of various adsorption sites on the sorbent surface such as

hydrophobic chain (methylene and benzenoid rings), ion exchanger fragments (N and O groups), hydrogen bonding sites (OH and NH) and pores which are ready to capture TC molecules [42].

The adsorbent amount is the main factor affecting the adsorption process since inefficient interaction at low adsorbent dosage causes low efficiency besides, high adsorbent dosage may shield the binding sites from analyte [43]. Hence the amount of adsorbent (5–15 mg) was also selected as a variable. It is observed from the 3D plots that the removal efficiencies increased as the dosages of sorbents increased which confirmed the increase of active binding sites and active surface area population on the solution. The effect of ionic strength was studied in the range of 1.0%–5.0% (m/v). It was found that adsorption of TC decreased upon addition of  $NaNO_3$  salt. Based on this observation, it can be concluded that attractive electrostatic forces are the main adsorption mechanism for TC interaction with the adsorbent and presence of high salt concentration depresses the analyte

Table 2  
ANOVA calculations for TC adsorption onto magnetic mesoporous carbon

Source	Sum of square	df	Mean square	F-value	p-value Prob > F	
Model	3,260.15	22	148.19	53.86	<0.0001	Significant
A-pH	47.75	1	47.75	17.36	0.0059	
B-Time	25.00	1	25.00	9.09	0.0236	
C-Dosage	160.02	1	160.02	58.16	0.0003	
D-Ionic	13.32	1	13.32	4.84	0.0700	
AB	5.09	1	5.09	1.85	0.2229	
AC	9.61	1	9.61	3.49	0.1108	
AD	13.03	1	13.03	4.74	0.0724	
BC	13.07	1	2,028.15	4.75	0.0721	
BD	9.92	1	66.99	3.61	0.1063	
CD	71.06	1	71.06	25.83	0.0023	
A <sup>2</sup>	1,534.99	1	1,534.99	557.94	<0.0001	
B <sup>2</sup>	42.83	1	42.83	15.57	0.0076	
C <sup>2</sup>	2.71	1	2.71	0.99	0.3590	
D <sup>2</sup>	27.47	1	27.47	9.99	0.0196	
A <sup>2</sup> B	39.92	1	39.92	14.51	0.0089	
A <sup>2</sup> C	110.86	1	110.86	40.29	0.0007	
A <sup>2</sup> D	5.06	1	5.06	1.84	0.2240	
AB <sup>2</sup>	7.39	1	7.39	2.69	0.1523	
AC <sup>2</sup>	1.44	1	1.44	0.53	0.4959	
B <sup>2</sup> C	24.54	1	24.54	8.92	0.0244	
B <sup>2</sup> D	0.77	1	0.77	0.28	0.6160	
BC <sup>2</sup>	0.96	1	0.96	0.35	0.5764	
Residual	16.51	6	2.75			
Lack of Fit	1.28	2	0.64	0.17	0.8507	Not significant
Pure error	15.23	4	3.81			
Cor total	3,276.66	28				

interaction with the sorbent surface. To evaluate the accuracy of the results obtained by the model, under optimum condition (pH, 5.5; contact time, 7.0 min; sorbent dose, 14 mg; and ionic strength, 4%), three experiments were carried out at initial TC concentration of 10.0 mg/L and results showed a good agreement between the optimum-calculated response (97%) and mean experimental response (95%).

3.3. Fitting of the oxidation process models

The empirical relationship between removal percentage (R%) and the variables in the oxidation process was decoded by the following equation:

$$R\% = 74.22 + 21.46A + 6.55B + 33.78C + 2.78AB + 20.01AC + 8.13BC - 22.32A^2 - 9.13B^2 - 30.36C^2 \quad (6)$$

In this equation, R% is the response (removal percentage); A, B, and C are dosage, contact time, and H<sub>2</sub>O<sub>2</sub> amount as independent variables. To compare the performances of adsorption/oxidation process, the solution pH and ionic strength were fixed at 5.5% and 4%, same to adsorption experiments. In other words, according to results of

adsorption experiment, TC concentration on the sorbent surface is in maximum level at the mentioned pH and ionic strength hence this value was selected for the oxidation process. The ANOVA calculations are shown in Table 3. The F value is 87.53 with a low probability value of p < 0.0001 and confirmed that TC oxidation process was statistically significant. Based on the p-values of each model term, only the interactive coefficient of AB is not significant on the TC oxidation. The value of R<sup>2</sup> and adjusted R<sup>2</sup> are 0.99 and 0.98 which indicated a high correlation between the observed and the predicted values of the response. Moreover, the signal to noise ratio of 30.99 demonstrated the significance of the model.

The NPP at Fig. 9a represents the normality of the data. At perturbation plot (Fig. 9b), steep curvature in the curves confirmed that TC oxidation efficiency is very sensitive to three factors. Moreover, the relationship between the predicted values of the response (%R) with observed R% in Fig. 9c shows good agreement with them. The three-dimensional response surfaces in Fig. 10 indicate that the removal percentage is very sensitive to catalyst dosage and H<sub>2</sub>O<sub>2</sub> amount since the increase in the value of these parameters causes an increase in removal efficiency. To evaluate

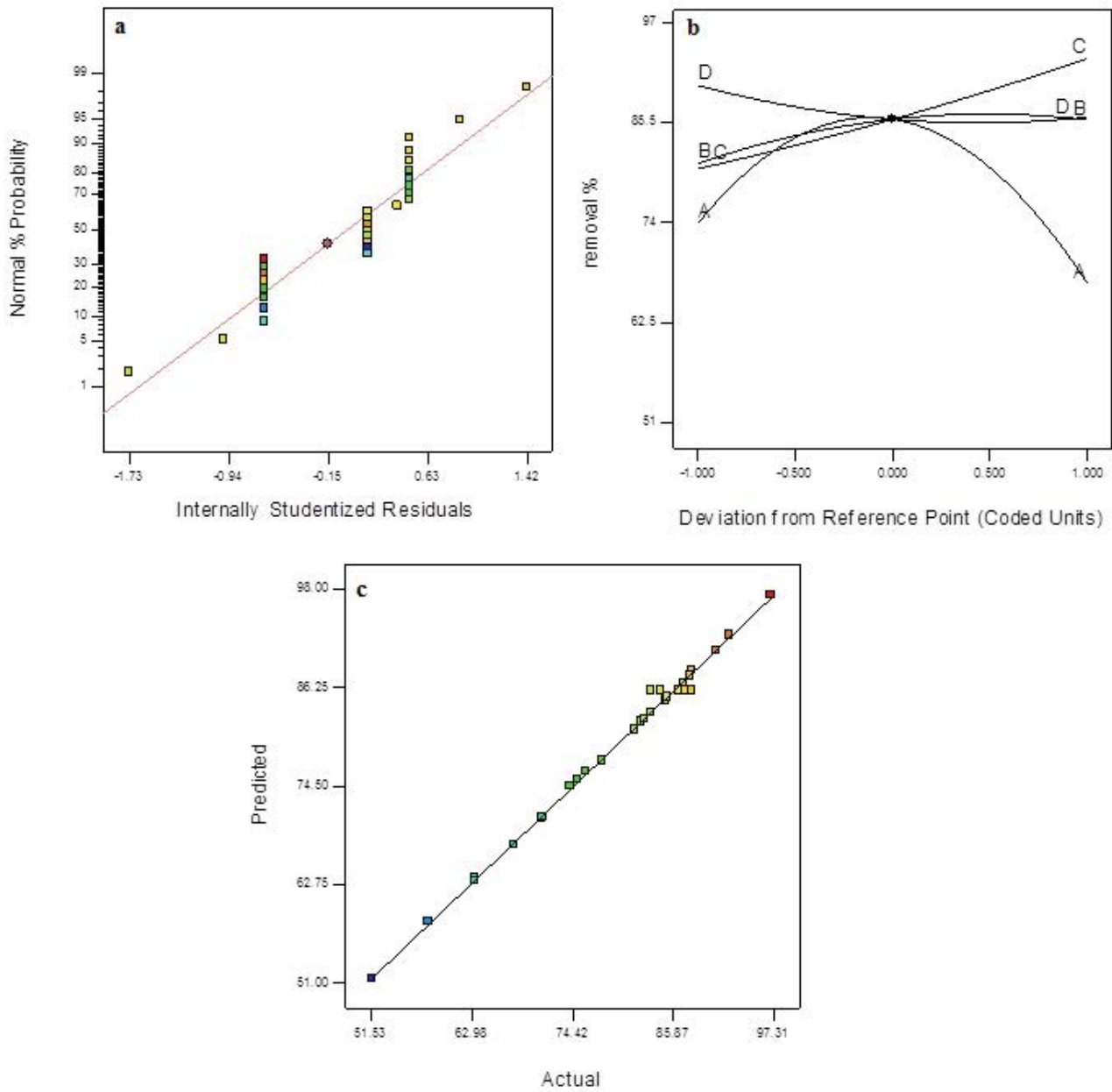


Fig. 6. NNP (a), perturbation (b) and predicted data vs. actual (c) for TC adsorption by the nanocomposite.

the accuracy of the results obtained by the model, under optimum condition (dosage of 7 mg; contact time, 10 min; and H<sub>2</sub>O<sub>2</sub> amount of 0.37 mL; H<sub>2</sub>O<sub>2</sub>/TC ratio of 1,000) three experiments were carried out at the initial TC concentration of 100 mg/L (20 mL) and results showed a good agreement between the optimum-calculated response (100 %) and mean experimental response (98%).

### 3.4. Kinetic study

To quantify the effect of time on TC adsorption four kinetic models including pseudo-first-order, pseudo-second-order, intraparticle diffusion, and liquid film were used based on the linearized equations:

$$\ln(Q_c - Q_t) = \ln Q_c - K_1 t \tag{7}$$

$$\frac{t}{Q_t} = \frac{1}{(K_2 Q_c^2)} + \left(\frac{1}{Q_c}\right) t \tag{8}$$

$$Q_t = K_f t^{0.5} + C \tag{9}$$

$$\ln(1 - F) = -K_{fd} t + C \tag{10}$$

In these equations,  $K_1$ ,  $K_2$ ,  $Q_c$ , and  $Q_t$  are the pseudo-first-order adsorption rate constant (min<sup>-1</sup>), the second-order rate

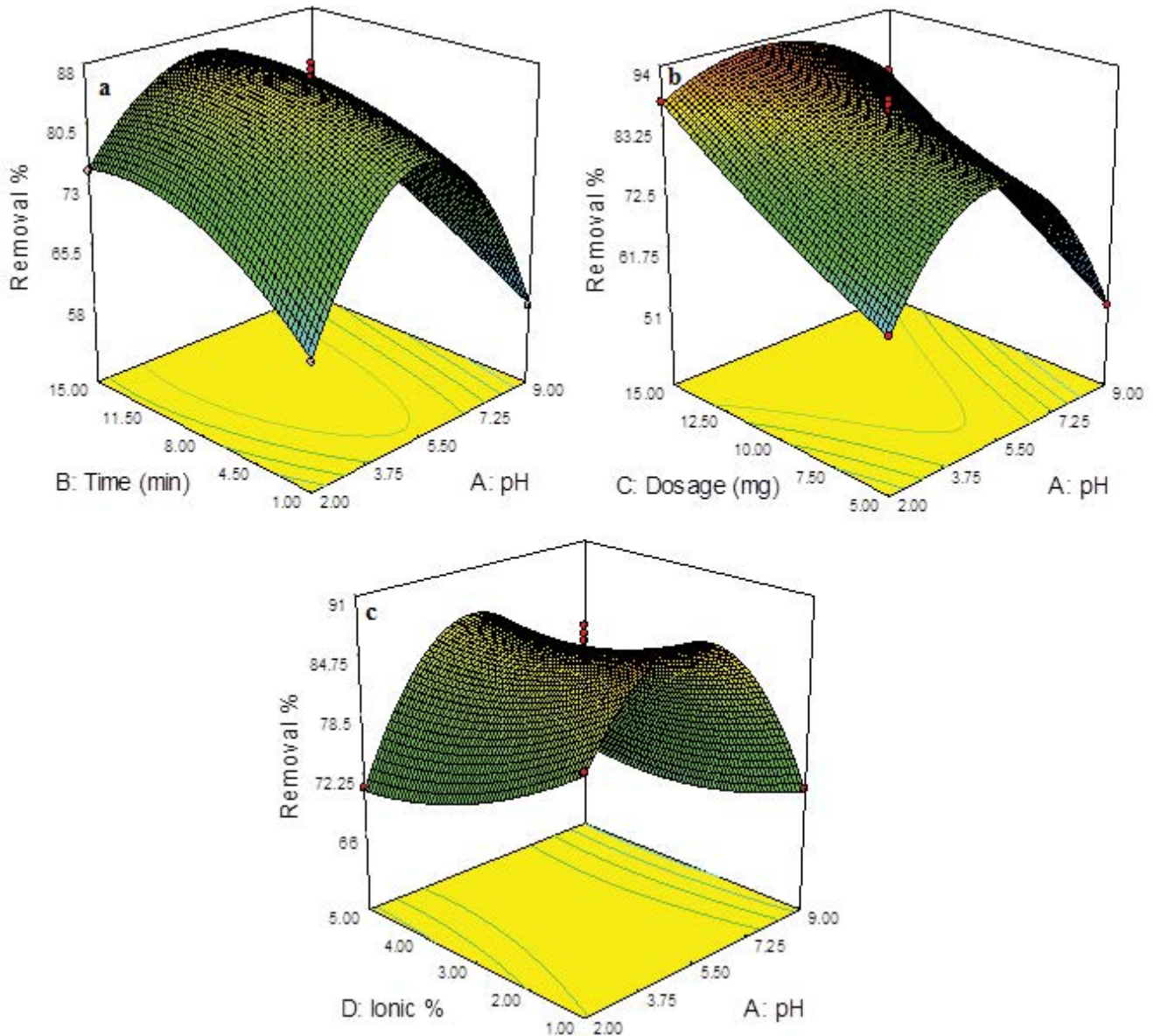


Fig. 7. 3D plots pH–time (a), dosage–pH (b), and ionic strength–pH (c) for TC adsorption.

constant ( $\text{g mg}^{-1} \text{min}^{-1}$ ), the values of the amount adsorbed per unit mass at equilibrium and at any time  $t$ , respectively. Moreover,  $K_i$  and  $K_{fd}$  are the adsorption rate constants and  $F$  is the fractional attainment of equilibrium ( $F = Q_t/Q_e$ ) [44,45]. Results are shown in Table 4 and Fig. 11. It can be seen that Lagergren plot of pseudo-first-order model (Eq. (7)) show higher linearity than the pseudo-second-order model (Eq. (8)) moreover the value of  $Q_e$  based on the pseudo-first-order plot had a lower deviation with those obtained from the experimental data. This result confirmed that the pseudo-first-order kinetic model can better describe TC adsorption onto the adsorbent.

The intraparticle diffusion model (Eq. (9)) was linear for the adsorption process but show a high intercept which confirmed that the intraparticle diffusion was not the rate-limiting step. The liquid film diffusion model (Eq. (10))

explains the role of transport of the adsorbate from the liquid phase up to the solid-phase boundary. It can be seen that the liquid film model of magnetic carbon composite has good linearity with small intercept value and proved that transport of the molecules to the sorbent surface is a kinetic controlling step.

### 3.5. Adsorption isotherms

The effects of TC concentrations on adsorption process have been analyzed in terms of Langmuir, Freundlich, Dubinin–Radushkevich (D–R), and Temkin isotherm equations (Eqs. (11)–(14)):

$$\frac{C_e}{Q_e} = \frac{1}{(Q_m b)} + \frac{C_e}{Q_m} \tag{11}$$

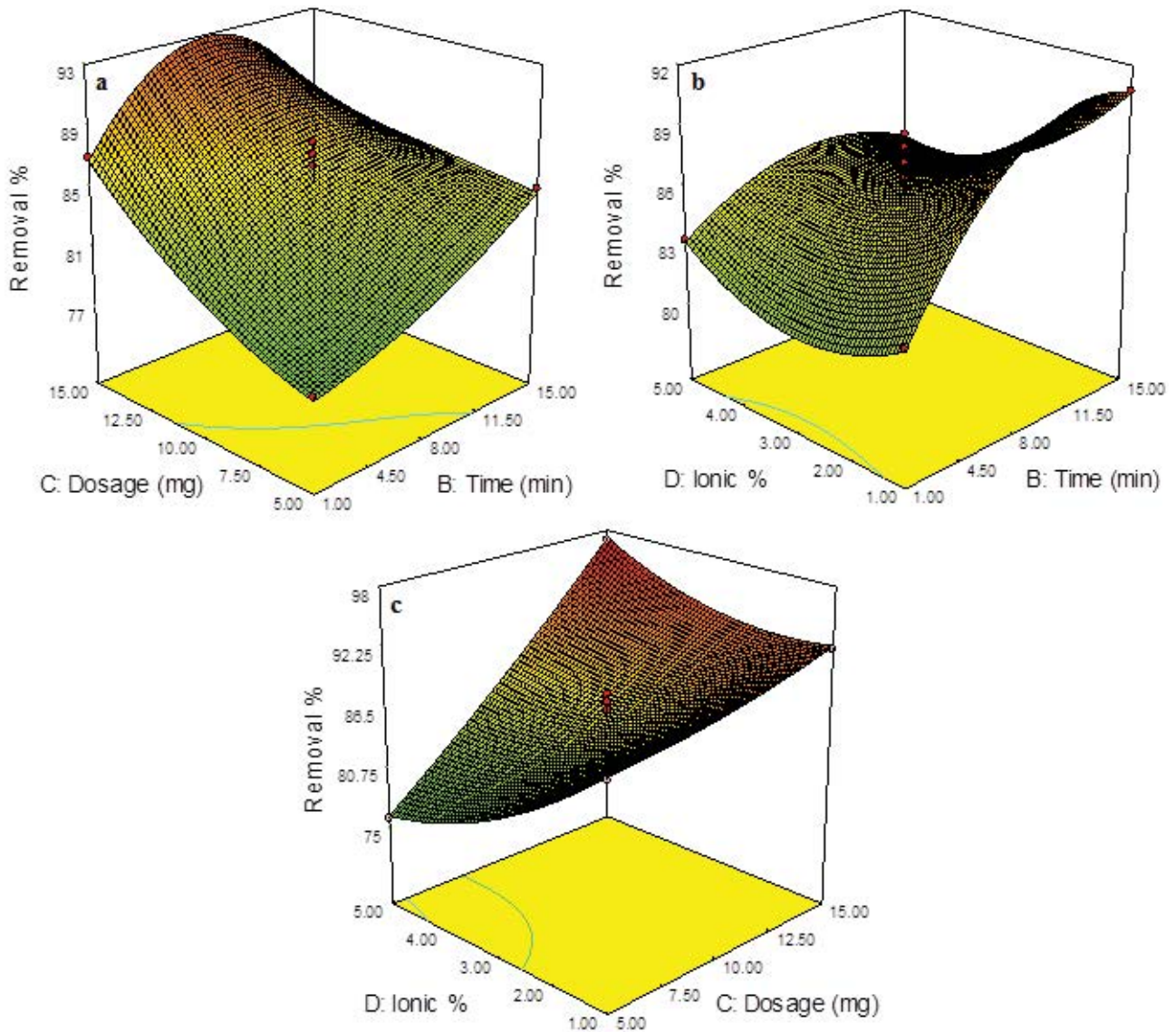


Fig. 8. 3D plots of dosage–time (a), ionic strength–time (b), and ionic strength–time (c) for TC adsorption.

$$\ln Q_e = \ln K_f + \frac{1}{n} \ln C_e \tag{12}$$

$$\ln Q = \ln Q_{\max} - \beta \varepsilon^2 \tag{13}$$

$$Q_e = B \ln A_T + B \ln C_e \tag{14}$$

where  $Q_e$  is the amount of TC sorbed per unit mass of the sorbent and  $C_e$  the amount of TC in the liquid phase at equilibrium.  $Q_m$ ,  $b$ , and  $K_f$ ,  $n$  are the Langmuir and Freundlich coefficients, respectively [28]. The  $\beta$  is the activity coefficient related to sorption energy and  $\varepsilon$  is the Polanyi potential [29,30], that can be calculated as follows:

$$\varepsilon = RT \ln \left( 1 + \frac{1}{C_e} \right) \tag{15}$$

At this equation,  $R$  is the gas constant (8.314 kJ/mol K) and  $T$  is the absolute temperature (K). The constant of  $\beta$  is used to calculate mean sorption energy ( $E$ ) by (Eq. (16)).  $E$  is defined as the free energy transfer of 1 mol of solute from the infinity of the surface of the sorbent.

$$E = \frac{1}{(2\beta)^{1/2}} \tag{16}$$

Temkin model (Eq. (14)) assumes that the heat of adsorption of all molecules in the layer would decrease linearly rather than logarithmic with coverage [46]. At the equation  $A_T$  is Temkin isotherm equilibrium binding constant (L/g),  $R$ , which is universal gas constant (8.314 J/mol/K), represent the temperature at 298 K and  $B$  is constant related to the heat of sorption (J/mol) [47].

The Langmuir plot (Fig. 12a) had good linearity with the monolayer capacity of 103.1 mg/g; furthermore,  $R_L$  value

Table 3  
ANOVA calculations for TC oxidation onto magnetic mesoporous carbon

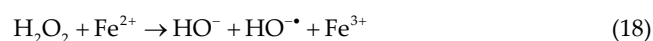
Source	Sum of square	df	Mean square	F-value	p-value Prob > F	
Model	23,470.28	11	2,133.66	87.53	<0.0001	Significant
A-Dosage	1,842.56	1	1,842.56	75.59	0.0003	
B-Time	342.96	1	342.96	14.07	0.0133	
H <sub>2</sub> O <sub>2</sub>	4,563.00	1	4,563.00	187.18	<0.0001	
AB	30.91	1	30.91	1.27	0.3112	
AC	1,602.00	1	1,602.00	65.72	0.0005	
BC	264.06	1	264.06	10.83	0.0217	
A <sup>2</sup>	2,097.38	1	2,097.38	86.04	0.0002	
B <sup>2</sup>	351.07	1	351.07	14.40	0.0127	
C <sup>2</sup>	3,881.93	1	3,881.93	159.24	<0.0001	
A <sup>2</sup> C	380.19	1	380.19	15.60	0.0109	
AB <sup>2</sup>	667.40	1	667.40	27.38	0.0034	
Residual	121.89	5	24.38			
Lack of fit	5.48	1	5.48	0.19	0.6868	Not significant
Pure error	116.41	4	29.10			
Cor. total	23,592.17	16				

( $R_L = 1/1 + bC_i$ ) is between 0 and 1 which confirmed that the Langmuir isotherm is favorable. The Freundlich isotherm yielded a linear plot (Fig. 12b) and the values of the coefficients (Table 5) indicated that the sorbent had good potential to be used as an adsorbent for TC removal. Physical adsorption was approved with the value of  $B$  (19.24 J/mol) based on Temkin model (Fig. 12c) [48]. The results for D–R model (Fig. 12d) showed that the magnitude of  $E$  was 0.56 kJ/mol (lower than 8 kJ/mol) and confirmed that TC adsorption is also a physical process. Based on  $R^2$  values and statistic error analysis (root mean square error; RMSE), the adsorption experimental data yielded excellent fits in the following isotherms order Freundlich > Temkin > Langmuir > Dubinin–Radushkevich as a results TC adsorption followed a multilayer adsorption process.

### 3.6. Adsorption and oxidation mechanism

Organic molecules can interact with the sorbent surface through physical or chemical processes. According to the results of the kinetics studies, the TC adsorption followed pseudo-first-order model. Moreover, the isotherm study showed that the adsorption followed the multilayer process. Hence it can be concluded that TC sorption occurs along with physical interaction. Moreover, the results of Temkin and Dubinin–Radushkevich adsorption model confirmed the physical interaction of TC with the sorbent surface. The nanocomposite structure contains methylene groups originated from aromatic backbone; hence it can be concluded that hydrophobic interaction between C–H groups of TC and the surface of adsorbent is the main reason for the efficient uptake of it by the nanohybrid [49]. TC also has polar functional groups of hydroxyl and amine hence increases the hydrogen bonding ability of it with the nitrogen groups on the composite surface [50]. Morphology of adsorbent also has a main role in the adsorption process. According to the FESEM image and BET data, the synthesized mesoporous compound has a pore structure which can trap TC molecules.

Fenton oxidation process of organic compounds may be divided into two major groups. In the first group, organic species react with the reactive inorganic radical species such as HO<sup>•</sup>, HO<sub>2</sub><sup>•</sup>, O<sub>2</sub><sup>•-</sup>, and H<sub>2</sub>O<sub>2</sub> except for the Fe species. The second group is included Fe which has an effective role in the transformation of environmental organic contaminants such as dyes and drugs [51]. In fact, degradation of the organic compound might be attributed to the oxidation effect of Fe<sup>2+</sup> assisted oxygen which originated from Fe. The mechanism could be proposed as follows:



According to the mentioned equations, the radicals are formed through H<sub>2</sub>O<sub>2</sub> decomposition in the presence of Fe<sup>2+</sup> ions [52]. In other words, Fe acts as redox-active centers which accelerate HO production from the decomposition of H<sub>2</sub>O<sub>2</sub> [53]. Literature notes that TC is containing two amide and phenolic acidic functional groups and dimethylamine as one basic functional group [15]. The ring system of TC has a higher electronic density which promotes the attack of radical species. TC degradation includes hydroxylation, loss of N-methyl, hydroxyl and carboxyl groups and cleavage of benzene rings [54].

### 3.7. Desorption and reusability

To desorb the adsorbed TC from surfaces of carbon composite, 5 mL of methanol, ethanol, and NaOH/ethanol (2 mL of aqueous NaOH with a concentration of 0.1 mol/L in 3 mL of ethanol) were studied. On the other hand, according to results for the effect of pH, the adsorption of TC was

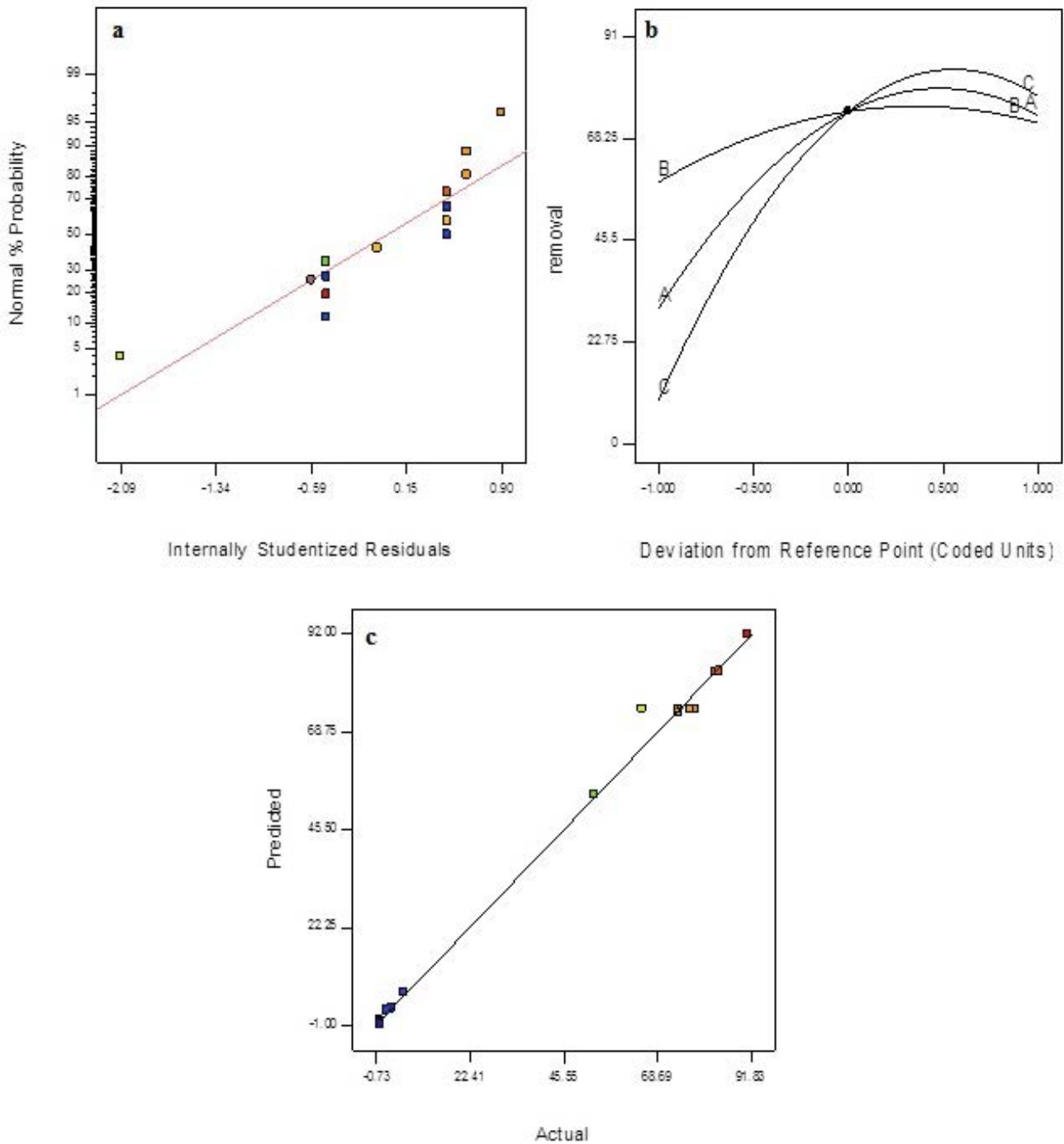


Fig. 9. NNP (a), perturbation (b) and predicted data vs. actual (c) for TC oxidation by the catalyst.

not efficient in the alkaline media. Therefore, elution with an alkaline solution and organic solvent may be favorable. It was found that alkaline ethanol solution shows maximum release (more than 95%) of TC after adsorption and oxidation process. A reusability experiment for TC adsorption was performed at an initial concentration of 10 mg/L and it was found that after three cycles of adsorption and desorption removal percentage decreased from 95% to 92% and 88%. However, oxidation efficiency at an initial concentration

of 100 mg/L was more than 95% after three cycles which decreased only 3% respect to initial removal efficiency (98%).

### 3.8. Comparison with literature

A comparison of TC adsorption and oxidation using the magnetic carbon composite was performed. Results are shown in Fig. 13. It can be seen that at an initial concentration of 10 mg/L adsorption efficiency is about 75%, however,

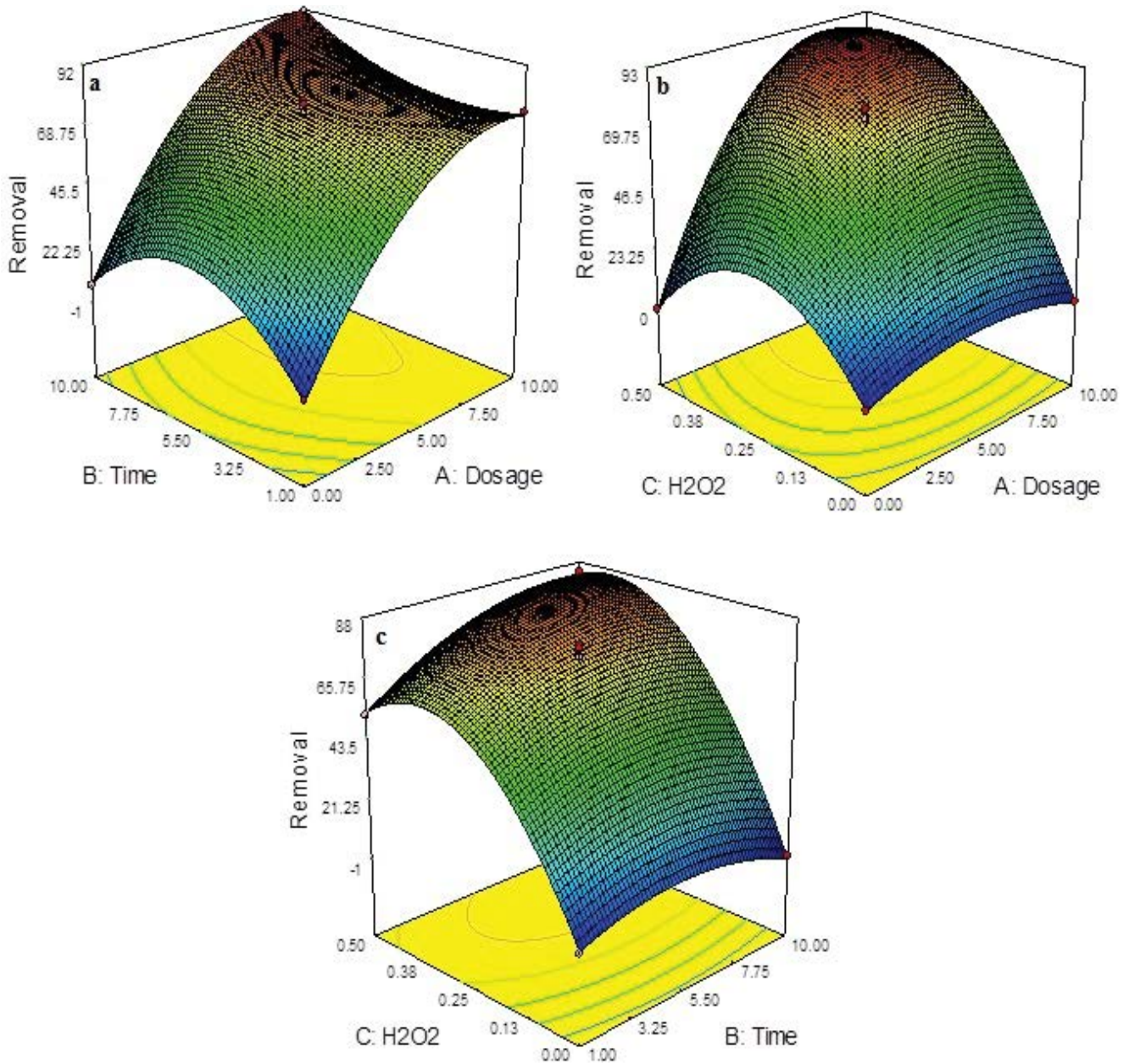


Fig. 10. 3D plots time–dosage (a), H<sub>2</sub>O<sub>2</sub>–dosage (b), H<sub>2</sub>O<sub>2</sub>–time (c) for TC oxidation.

Table 4  
Data of kinetic models for adsorption of TC using magnetic mesoporous carbon

	$R^2$	0.90		$R^2$	0.94
First order	$K_1$	0.31	Diffusion model	$K_i$	33.81
	$Q$	85.05		$C$	7.23
	$R^2$	0.81		$R^2$	0.90
Second order	$K_2$	0.0015	Liquid film	$K_{fd}$	0.318
	$Q$	135.13		$C$	0.0011
	$Q_{exp}$	85			

the oxidation process showed removal percentage of more than 99%. With the increase of initial concentration up to 100 mg/L adsorption removal decreased to 28.5% but oxidation process shows removal of 91%. The performance of the presented removal system was compared with some reports in the literature (Table 6) based on equilibrium time, adsorption capacity and adsorption conditions (concentration range). According to results, the prepared adsorbent in this work showed very fast adsorption equilibrium comparing with the reported works. Fast equilibrium time confirmed the external surface adsorption and absence of internal diffusion resistance for TC adsorption. The magnetic carbon composite also shows higher adsorption capacity and

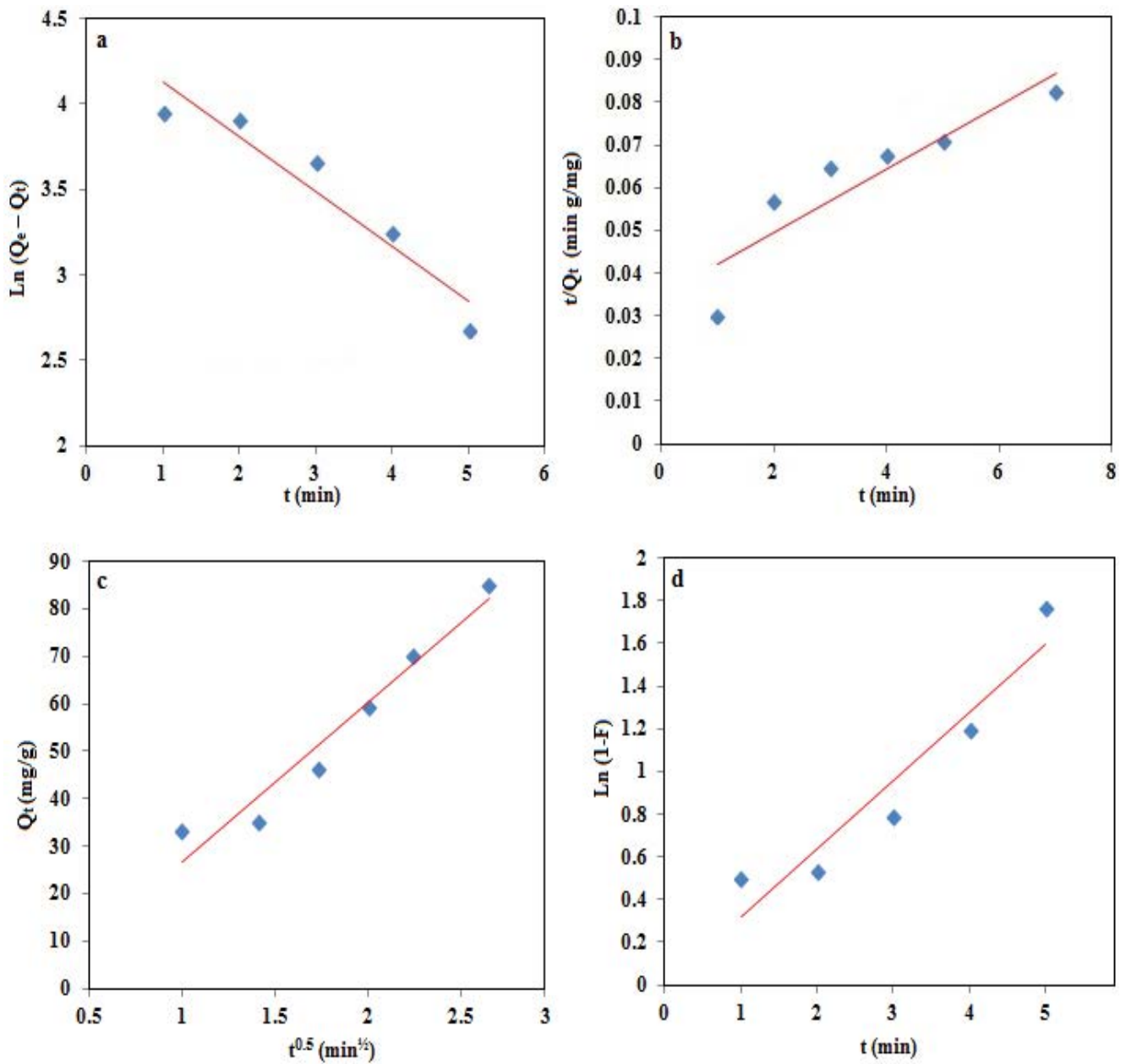


Fig. 11. Pseudo-first-order (a), pseudo-second-order (b), intraparticle diffusion (c) and liquid film model (d).

lower adsorbent dosage in comparison with some reports in Table 6. As a result, as synthesized sorbent appears to be a promising adsorbent for the removal of emerging micro-pollutants from aqueous solutions.

Oxidation process can be performed through several routes. In other words, employing metal ions, metal nanoparticles, use of  $H_2O_2$ , and  $H_2O_2$ /metal nanoparticles are some of the most employed routes of TC oxidation. Wang et al. [55] used  $Fe^{3+}$  ions for TC oxidation. This method is efficient but required high concentration of  $Fe^{3+}$  ions (1–13 mg/L) which causes secondary pollution of water by the metal ions. Other approaches include use of metal nanoparticles which has been employed by Cao et al. [56]. This route must be used at acidic solution which

causes leaching of metal ions to the solution as secondary pollutant. Employment of  $H_2O_2$  is another method which was used by Chen et al [54]. At this experiment, high concentration of hydrogen peroxide is required; moreover, the reaction is completed after 120 min. These limitations can be removed by employing  $H_2O_2$ /metal nanoparticles [57] as presented at this work. This process uses the ability of nanoparticles to enhance the production rate of hydroxyl radical through Fenton catalytic process which caused decrease in the reaction time as well as amount of used  $H_2O_2$ . Moreover, this process occurs at low acidic medium (pH over than 5). This situation induces iron oxide formation which removes Fe ions from the solution and reduces secondary pollution of the metal ions.

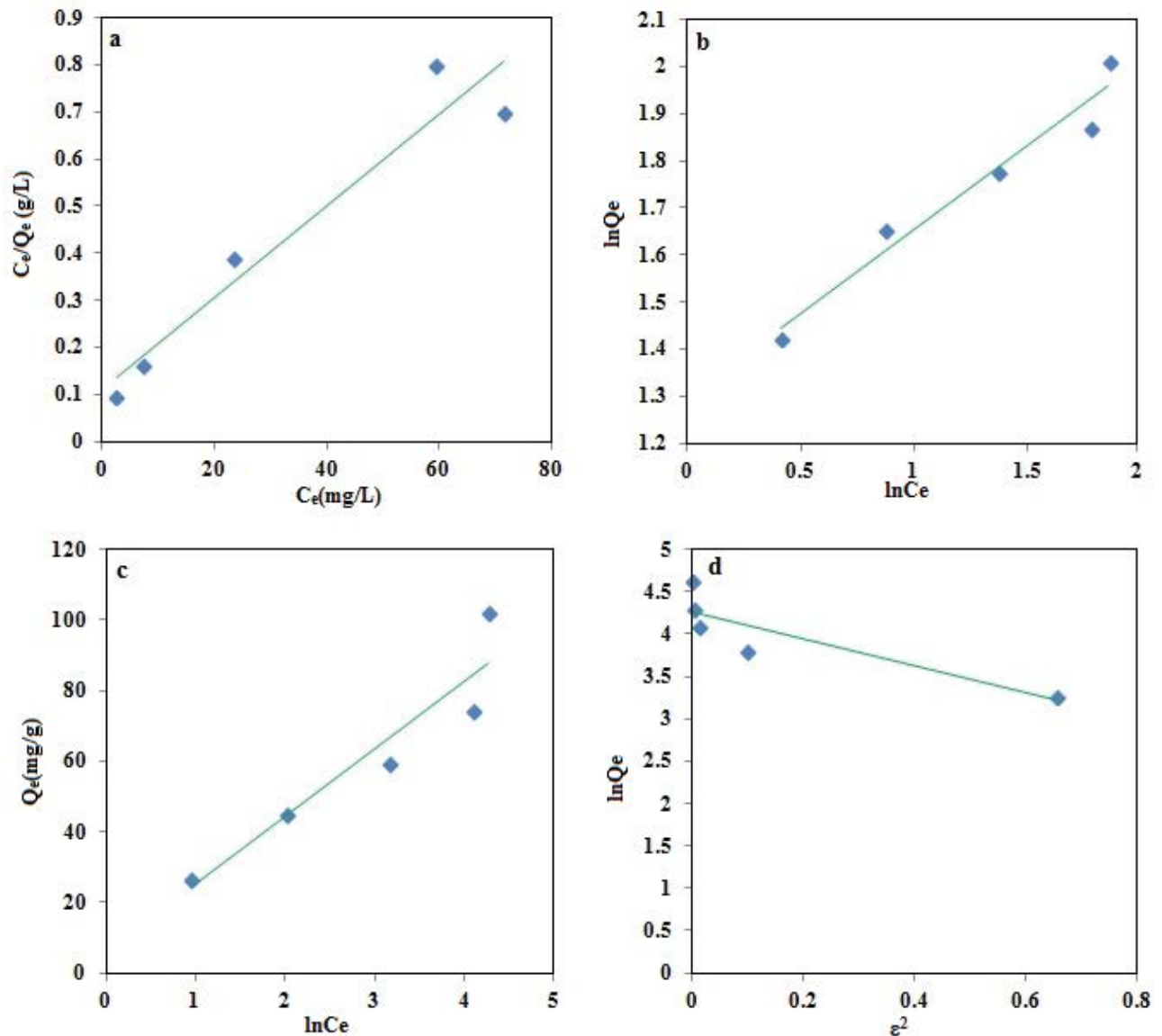


Fig. 12. Langmuir isotherm (a), Freundlich isotherm (b), Temkin isotherm (c), and D-R isotherm model for TC adsorption.

#### 4. Conclusions

In this work, an efficient magnetic carbon composite was developed based on Mn-Fe - polyphenol and employed for tetracycline removal. The synthesis process was based on the heat treatment of  $MnFe_2O_4$  - polyphenol derivative as a precursor. The prepared composite showed a porous structure with zero-valent iron nanoparticles as a magnetic fragment of the nanocomposite. The prepared composite was used for TC removal through two different route, that is, adsorption and oxidation with the aid of RSM for optimizing effective parameters. Kinetic and isotherm study for the adsorption process was performed and it was found that TC adsorption followed the Freundlich isotherm model along with the pseudo-first-order kinetic model. Equilibrium time of 7.0 and 10 min was obtained for adsorption and oxidation process, respectively. Moreover, at the initial TC concentration of 10–100 mg/L, the maximum adsorption capacity of 103.1

and 333 mg/g was obtained by adsorption and oxidation process, respectively. According to the results, it can be seen that adsorption process shows lower equilibrium time as well as the sorbent can be reused. Besides oxidation process showed higher adsorption capacity relative to adsorption. It can be concluded that by using the prepared nanocomposite, TC removal with the aid of oxidation is more efficient than adsorption process. Owing to the presence of various functional groups on the structure of the prepared composite, it has potential to be employed for removal of organic and inorganic pollutants such as dyes and heavy metals.

#### Acknowledgment

Support for this study by the Research Council of the University of Tehran and Zanjan through grants is gratefully acknowledged.

Table 5  
Data of isotherm models for TC adsorption onto magnetic mesoporous carbon

Models	Parameters	Values
Langmuir	$R^2$	0.93
	$Q_m$	103.1
	$b$	0.086
	$R_L$	0.10–0.53
	RMSE	12.62
Freundlich	$R^2$	0.95
	$n$	2.81
	$K_f$	19.90
	RMSE	9.35
D-R	$R^2$	0.76
	$Q_m$	70.92
	$E$	0.56
	RMSE	14.65
Temkin	$R^2$	0.89
	$A_T$	1.34
	$B_T$	19.24
	RMSE	9.87

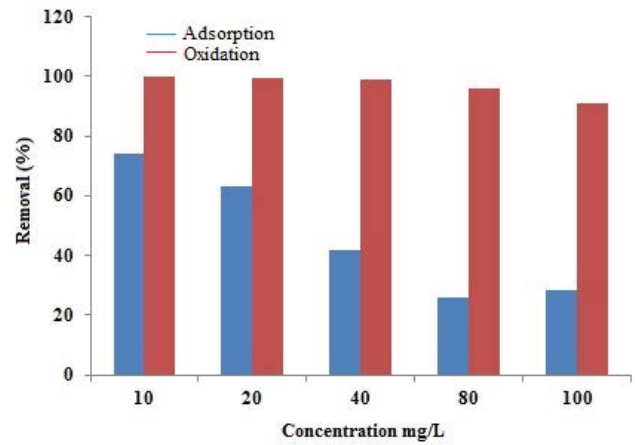


Fig. 13. Comparison of TC adsorption and oxidation efficiency of the nanocomposite (conditions: TC concentration 10–100 mg/L, pH = 5.5, sample volume 20 mL, contact time, 10.0 min; sorbent dose, 14 mg, catalyst dosage 7 mg).

Table 6  
Comparison TC adsorption property of prepared composite with some sorbents

Adsorbent	Maximum capacity (mg g <sup>-1</sup> )	Equilibrium time (min)	Dosage mg/mL	Concentration mg/L	References
Graphene oxide	313	90	0.18	8–166	[1]
Porous activated carbon	897	17 h	0.1	60–200	[3]
Activated carbon	625	24 h	0.2	200–400	[4]
Crystalline nanocellulose	7.73	300	1.5	1–50	[5]
Amino-Fe (III) - SBA15	96.91	300	1.0	4–80	[6]
Fe <sub>3</sub> O <sub>4</sub> @graphene	423	50	1.2	–	[9]
MCM-41 - Fe	526.3	60	1.0	10–500	[12]
Activated carbon	375.4	8 d	1.0	100–1,000	[50]
<sup>a</sup> Magnetic carbon	103.1	7.0	0.70	10–100	This work
<sup>b</sup> Magnetic carbon	333	10	0.35	10–100	This work

<sup>a</sup>Adsorption.

<sup>b</sup>Oxidation.

## References

- [1] Y. Gao, Y. Li, L. Zhang, H. Huang, J. Hu, S. Mazhar, X. Su, Adsorption and removal of tetracycline antibiotics from aqueous solution by graphene oxide, *J. Colloid Interface Sci.*, 368 (2012) 540–546.
- [2] Y. Wang, H. Zhang, J. Zhang, C. Lu, Q. Huang, J. Wu, F. Liu, Degradation of tetracycline in aqueous media by ozonation in an internal loop-lift reactor, *J. Hazard. Mater.*, 192 (2011) 35–43.
- [3] D. Zhang, J. Yin, J. Zhao, H. Zhu, C. Wang, Adsorption and removal of tetracycline from water by petroleum coke-derived highly porous activated carbon, *J. Environ. Chem. Eng.*, 3 (2015) 1504–1512.
- [4] F. Güzel, H. Say, Adsorptive efficacy analysis of novel carbonaceous sorbent derived from grape industrial processing wastes towards tetracycline in aqueous solution, *J. Taiwan Inst. Chem. Eng.*, 60 (2016) 236–240.
- [5] M. Rathod, S. Haldar, S. Basha, Nanocrystalline cellulose for removal of tetracycline hydrochloride from water via biosorption: equilibrium, kinetic and thermodynamic studies, *Ecol. Eng.*, 84 (2015) 240–249.
- [6] Z. Zhang, H. Lan, H. Liu, J. Qu, Removal of tetracycline antibiotics from aqueous solution by amino-Fe (III) functionalized SBA15, *Colloids Surf., A*, 471 (2015) 133–138.
- [7] J. Jinhui, L. Kuili, F. Weiqiang, L. Meng, L. Yu, M. Baodong, B. Hongye, S. Hongqiang, Y. Songliu, S. Weidong, Electrospinning synthesis and photocatalytic property of Fe<sub>2</sub>O<sub>3</sub>/MgFe<sub>2</sub>O<sub>4</sub> heterostructure for photocatalytic degradation of tetracycline, *Mater. Lett.*, 176 (2016) 1–4.
- [8] C.H. Huang, K.P. Chang, H. De Ou, Y.C. Chiang, C.F. Wang, Adsorption of cationic dyes onto mesoporous silica, *Microporous Mesoporous Mater.*, 141 (2011) 102–109.
- [9] Y. Zhang, Z. Jiao, Y. Hu, S. Lv, H. Fan, Y. Zeng, Removal of tetracycline and oxytetracycline from water by magnetic

- Fe<sub>3</sub>O<sub>4</sub>@graphene, *Environ. Sci. Pollut. Res.*, 24 (2017) 2987–2995.
- [10] Y. Chen, L. Ding, J. Nie, Isotherm and thermodynamic studies of the biosorption of lead, cadmium and copper from aqueous solutions by rice bran, *Desal. Wat Treat.*, 44 (2012) 168–173.
- [11] M.B. Ahmed, J.L. Zhou, H.H. Ngo, W. Guo, Adsorptive removal of antibiotics from water and wastewater: progress and challenges, *Sci. Total Environ.*, 532 (2015) 112–126.
- [12] Y. Guo, W. Huang, B. Chen, Y. Zhao, D. Liu, Y. Sun, Removal of tetracycline from aqueous solution by MCM-41-zeolite A loaded nano zero valent iron: synthesis, characteristic, adsorption performance and mechanism, *J. Hazard. Mater.*, 339 (2017) 22–32.
- [13] M.H. Beyki, H. Alijani, Y. Fazli, Solvent free synthesized MnFe<sub>2</sub>O<sub>4</sub>@polyamid resin as a novel green nanohybrid for fast removing Congo red, *J. Mol. Liq.*, 216 (2016) 6–11.
- [14] H. Hadoun, Z. Sadaoui, N. Souami, D. Sahel, I. Toumert, Characterization of mesoporous carbon prepared from date stems by H<sub>3</sub>PO<sub>4</sub> chemical activation, *Appl. Surf. Sci.*, 280 (2013) 1–7.
- [15] Y. Zhai, Y. Dou, X. Liu, S.S. Park, C.S. Ha, D. Zhao, Soft-template synthesis of ordered mesoporous carbon/nanoparticle nickel composites with a high surface area, *Carbon*, 49 (2011) 545–555.
- [16] Z. Xie, D. Sheng, Ionic liquid based approaches to carbon materials synthesis, *Eur. J. Inorg. Chem.*, 2015 (2015) 1137–1147.
- [17] D. Carriazo, M.C. Guti, M.L. Ferrer, F. Monte, Resorcinol-based deep eutectic solvents as both carbonaceous precursors and templating agents in the synthesis of hierarchical porous carbon monoliths, *Chem. Mater.*, 22 (2010) 6146–6152.
- [18] Y.W. You, E.H. Moon, I. Heo, H. Park, J.S. Hong, J.K. Suh, Preparation and characterization of porous carbons from ion-exchange resins with different degree of cross-linking for hydrogen storage, *J. Ind. Eng. Chem.*, 45 (2017) 164–170.
- [19] R. Li, A. Cao, Y. Zhang, G. Li, F. Jiang, S. Li, D. Chen, C. Wang, J. Ge, C. Shu, Formation of nitrogen-doped mesoporous graphitic carbon with the help of melamine, *ACS Appl. Mater. Interfaces*, 6 (2014) 20574–20578.
- [20] D. Hulicova, J. Yamashita, Y. Soneda, H. Hatori, M. Kodama, Supercapacitors prepared from melamine-based carbon, *Chem. Mater.*, 17 (2005) 1241–1247.
- [21] J. Wei, D. Zhou, Z. Sun, Y. Deng, Y. Xia, D. Zhao, A controllable synthesis of rich nitrogen-doped ordered mesoporous carbon for CO<sub>2</sub> capture and supercapacitors, *Adv. Funct. Mater.*, 23 (2013) 2322–2328.
- [22] M.J. Pirouzi, M.H. Beyki, F. Shemirani, Anhydride functionalized calcium ferrite nanoparticles: a new selective magnetic material for enrichment of lead ions from water and food samples, *Food Chem.*, 170 (2015) 131–137.
- [23] N. Farzin Nejad, E. Shams, M.K. Amini, J.C. Bennett, Synthesis of magnetic mesoporous carbon and its application for adsorption of dibenzothiophene, *Fuel Process. Technol.*, 106 (2013) 376–384.
- [24] H. Liu, Y. Yang, J. Kang, M. Fan, J. Qu, Removal of tetracycline from water by Fe-Mn binary oxide, *J. Environ. Sci.*, 24 (2012) 242–247.
- [25] L. Shao, Z. Ren, G. Zhang, L. Chen, Facile synthesis, characterization of a MnFe<sub>2</sub>O<sub>4</sub>/activated carbon magnetic composite and its effectiveness in tetracycline removal, *Mater. Chem. Phys.*, 135 (2012) 16–24.
- [26] J. Chen, T. Xu, J. Ding, Y. Ji, P. Ni, Z. Li, Mn – Ce – Co complex oxide nanoparticles: hydrothermal synthesis and their catalytic subcritical oxidation of 4, 4-Dibromobiphenyl, *J. Hazard. Mater.*, 235–236 (2012) 85–91.
- [27] H. Bel Hadjltaief, P. Da Costa, P. Beaunier, M.E. Gálvez, M. Ben Zina, Fe-clay-plate as a heterogeneous catalyst in photo-Fenton oxidation of phenol as probe molecule for water treatment, *Appl. Clay Sci.*, 91–92 (2014) 46–54.
- [28] J.P. Pouget, M.E. Jozefowicz, J. Epstein, X. Tang, G. MacDiarmid, X-ray structure of polyaniline, *Macromolecules*, 24 (1991) 779–789.
- [29] H. Alijani, M.H. Beyki, Z. Shariatnia, M. Bayat, F. Shemirani, A new approach for one step synthesis of magnetic carbon nanotubes/diatomite earth composite by chemical vapor deposition method: application for removal of lead ions, *Chem. Eng. J.*, 253 (2014) 456–463.
- [30] R. Snovski, J. Grinblat, M.T. Sougrati, J.C. Jumas, S. Margel, Synthesis and characterization of iron, iron oxide and iron carbide nanostructures, *J. Magn. Magn. Mater.*, 349 (2014) 35–44.
- [31] H. Yan, J. Zhang, C. You, Z. Song, B. Yu, Y. Shen, Influences of different synthesis conditions on properties of Fe<sub>3</sub>O<sub>4</sub> nanoparticles, *Mater. Chem. Phys.*, 113 (2009) 46–52.
- [32] M.H. Beyki, H. Alijani, Y. Fazli, Optimization using response surface methodology for fast removal of hazardous azo dye by  $\gamma$ -Fe<sub>2</sub>O<sub>3</sub>@CuO nanohybrid synthesized by sol-gel combustion, *Res. Chem. Intermed.*, 43 (2017) 6245–6257.
- [33] S.H. Hosseini, A. Asadnia, Synthesis, Characterization, and Microwave-absorbing properties of polypyrrole/MnFe<sub>2</sub>O<sub>4</sub> nanocomposite, *J. Nanomater.*, 2012 (2012) 1–6.
- [34] M. Khairy, M.E. Gouda, Electrical and optical properties of nickel ferrite/polyaniline nanocomposite, *J. Adv. Res.*, 6 (2015) 555–562.
- [35] M. Hossein, F. Shemirani, J. Malakootikhah, S. Minaeian, Catalytic synthesis of graphene-like polyaniline derivative - MFe<sub>2</sub>O<sub>4</sub> (M; Cu, Mn) nanohybrid as multifunctionality water decontaminant, *React. Funct. Polym.*, 125 (2018) 108–117.
- [36] M. Bayat, M.H. Beyki, F. Shemirani, One-step and biogenic synthesis of magnetic Fe<sub>3</sub>O<sub>4</sub>-Fir sawdust composite: application for selective preconcentration and determination of gold ions, *J. Ind. Eng. Chem.*, 21 (2015) 912–919.
- [37] M. Thommes, K. Kaneko, A.V. Neimark, J.P. Olivier, F. Rodriguez-reinoso, J. Rouquerol, K.S.W. Sing, Physisorption of gases, with special reference to the evaluation of surface area and pore size distribution (IUPAC Technical Report), *Pure Appl. Chem.*, 87 (2015) 1051–1069.
- [38] A. Dabrowski, Adsorption, from theory to practice, *Adv. Colloid Interface Sci.*, 93 (2001) 135–224.
- [39] M. Foroughi, A.R. Rahmani, G. Asgari, D. Nematollahi, K. Yetilmezsoy, Optimization of a three-dimensional electrochemical system for tetracycline degradation using Box-Behnken design, *Fresenius Environ. Bull.*, 27 (2019) 1914–1922.
- [40] M. Foroughi, S. Chavoshi, M. Bagheri, K. Yetilmezsoy, M. Taghi, Alum-based sludge (AbS) recycling for turbidity removal in drinking water treatment: an insight into statistical, technical, and health-related standpoints, *J. Mater. Cycles Waste Manage.*, 20 (2018) 1999–2017.
- [41] R. Khani, S. Sobhani, M.H. Beyki, Highly selective and efficient removal of lead with magnetic nano-adsorbent: multivariate optimization, isotherm and thermodynamic studies, *J. Colloid Interface Sci.*, 466 (2016) 198–205.
- [42] M.H. Beyki, F. Feizi, F. Shemirani, Melamine-based dendronized magnetic polymer in the adsorption of Pb(II) and preconcentration of rhodamine B, *React. Funct. Polym.*, 103 (2016) 81–91.
- [43] N. Tumin, A. Chuah, Adsorption of copper from aqueous solution by Elais Guineensis kernel activated carbon, *J. Eng. Sci. Technol.*, 3 (2008) 180–189.
- [44] T.K. Naiya, A.K. Bhattacharya, S.K. Das, Clarified sludge (basic oxygen furnace sludge) - an adsorbent for removal of Pb(II) from aqueous solutions - kinetics, thermodynamics and desorption studies, *J. Hazard. Mater.*, 170 (2009) 252–262.
- [45] L. You, C. Huang, F. Lu, A. Wang, X. Liu, Q. Zhang, Facile synthesis of high performance porous magnetic chitosan - polyethylenimine polymer composite for Congo red removal, *Int. J. Biol. Macromol.*, 107 (2018) 1620–1628.
- [46] K.Y. Foo, B.H. Hameed, Insights into the modeling of adsorption isotherm systems, *Chem. Eng. J.*, 156 (2010) 2–10.
- [47] N. Ayawei, A.N. Ebelegi, D. Wankasi, Modelling and Interpretation of Adsorption Isotherms, *J. Chem.*, 2017 (2017) 1–11.
- [48] A. Dada, A. Olalekan, A. Olatunya, O. Dada, Langmuir, Freundlich, Temkin and Dubinin-Radushkevich isotherms studies of equilibrium sorption of Zn<sup>2+</sup> unto phosphoric acid modified rice husk, *IOSR J. Appl. Chem.*, 3 (2012) 38–45.
- [49] B. Pan, B. Xing, Adsorption mechanisms of organic chemicals on carbon nanotubes, *Environ. Sci. Technol.*, 42 (2008) 9005–9013.
- [50] J. Rivera-Utrilla, C.V. Gómez-Pacheco, M. Sánchez-Polo, J.J. López-Peñalver, R. Ocampo-Pérez, Tetracycline removal from

- water by adsorption / bioadsorption on activated carbons and sludge-derived adsorbents, *J. Environ. Manage.*, 131 (2013) 16–24.
- [51] N. Kang, D.S. Lee, J. Yoon, Kinetic modeling of Fenton oxidation of phenol and monochlorophenols, *Chemosphere*, 47 (2002) 915–924.
- [52] Y. Fu, L. Peng, Q. Zeng, Y. Yang, H. Song, J. Shao, S. Liu, High efficient removal of tetracycline from solution by degradation and flocculation with nanoscale zerovalent iron, *Chem. Eng. J.*, 270 (2015) 631–640.
- [53] B. Kakavandi, A. Takdastan, N. Jaafarzadeh, M. Azizi, A. Mirzaei, A. Azari, Application of  $\text{Fe}_3\text{O}_4@\text{C}$  catalyzing heterogeneous UV-Fenton system for tetracycline removal with a focus on optimization by a response surface method, *J. Photochem. Photobiol. A: Chem.*, 314 (2016) 178–188.
- [54] Y. Chen, Y. Ma, J. Yang, L. Wang, J. Lv, C. Ren, Aqueous tetracycline degradation by  $\text{H}_2\text{O}_2$  alone: removal and transformation pathway, *Chem. Eng. J.*, 307 (2017) 15–23.
- [55] H. Wang, H. Yao, P. Sun, J. Pei, D. Li, C. Huang, Chemosphere Oxidation of tetracycline antibiotics induced by Fe (III) ions without light irradiation, *Chemosphere*, 119 (2015) 1255–1261.
- [56] J. Cao, Z. Xiong, B. Lai, Effect of initial pH on the tetracycline (TC) removal by zero-valent iron: adsorption, oxidation and reduction, *Chem. Eng. J.*, 343 (2018) 492–499.
- [57] D. Fu, Z. Chen, D. Xia, L. Shen, Y. Wang, Q. Li, A novel solid digestate-derived biochar-Cu NP composite activating  $\text{H}_2\text{O}_2$  system for simultaneous adsorption and degradation of tetracycline, *Environ. Pollut.*, 221 (2017) 301–310.